2017

Internal Wave Scattering in Continental Slope Canyons, Part 1: Theory and Development of a Ray Tracing Algorithm

Robert Nazarian
Fairfield University, rnazarian@fairfield.edu

Sonya Legg

Published Citation

Nazarian, R. H., & Legg, S. (2017). Internal wave scattering in continental slope canyons, part 1: Theory and development of a ray tracing algorithm. Ocean modelling, 118, 1-15. https://doi.org/10.1016/j.ocemod.2017.07.002

Ocean Modelling 118 (2017) 1–15

Contents lists available at ScienceDirect

Ocean Modelling

journal homepage: www.elsevier.com/locate/ocemod

Internal wave scattering in continental slope canyons, part 1: Theory and development of a ray tracing algorithm

Robert H. Nazarian*, Sonya Legg

Program in Atmospheric and Oceanic Sciences, Princeton University, Princeton, NJ 08540, USA

ARTICLE INFO

Article history:
Received 21 February 2017
Revised 15 July 2017
Accepted 20 July 2017
Available online 3 August 2017

Keywords:
Internal waves
Canyons
Mixing
Ray tracing

ABSTRACT

When internal waves interact with topography, such as continental slopes, they can transfer wave energy to local dissipation and diapycnal mixing. Submarine canyons comprise approximately ten percent of global continental slopes, and can enhance the local dissipation of internal wave energy, yet parameterizations of canyon mixing processes are currently missing from large-scale ocean models. As a first step in the development of such parameterizations, we conduct a parameter space study of M2 tidal-frequency, low-mode internal waves interacting with idealized V-shaped canyon topographies. Specifically, we examine the effects of varying the canyon mouth width, shape and slope of the thalweg (line of lowest elevation). This effort is divided into two parts. In the first part, presented here, we extend the theory of 3-dimensional internal wave reflection to a rotated coordinate system aligned with our idealized V-shaped canyons. Based on the updated linear internal wave reflection solution that we derive, we construct a ray tracing algorithm which traces a large number of rays (the discrete analog of a continuous wave) into the canyon region where they can scatter off topography. Although a ray tracing approach has been employed in other studies, we have, for the first time, used ray tracing to calculate changes in wavenumber and ray density which, in turn, can be used to calculate the Froude number (a measure of the likelihood of instability). We show that for canyons of intermediate aspect ratio, large spatial envelopes of instability can form in the presence of supercritical sidewalls. Additionally, the canyon height and length can modulate the Froude number. The second part of this study, a diagnosis of internal wave scattering in continental slope canyons using both numerical simulations and this ray tracing algorithm, as well as a test of robustness of the ray tracing, is presented in the companion article.

1. Introduction

Internal waves are efficient transmitters of energy across ocean basins. These waves, either generated by the winds or tidal flows over rough topography (Munk and Wunsch, 1998) propagate through the ocean basins until they are forced to break by topographic features, or non-linear wave-wave interactions (MacKinnon et al., 2013). To first approximation, 30–60% of the initial wave energy makes it away from the generation site and previous studies have shown that a sizable portion of this energy can make it to the edge of the basins where the continental slope is encountered (St. Laurent and Nash, 2004; Klymak et al., 2006; Alford et al., 2011; Waterhouse et al., 2014). At these continental slopes, internal waves are scattered, leading to higher wavenumbers and/or greater energy density. They can then become unstable (due to shear instability, convective instability or some combination thereof), break and lead to diapycnal mixing. Diapycnal mixing due to internal tide breaking, both near the generation site and in the farfield, is an important component of the global meridional overturning circulation (Ilicak and Vallis, 2012; Talley, 2013).

Over the past two decades, there have been numerous studies aimed at understanding the parameter space for which internal waves break over a host of farfield topographies, as well as at the generation site itself (Legg and Klymak, 2008; Nikurashin and Legg, 2011; Johnston et al., 2011). Plane slopes (Cacchione and Wunsch, 1974; Ivey and Nokes, 1989; Hallock and Field, 2005; Nash et al., 2007; Kunze et al., 2012; Hall et al., 2013), convex and concave slopes (Legg and Adcroft, 2003), ridges and mounts (Johnston and Merrifield, 2003; Klymak et al., 2013), channels (Drijfhout and Maas, 2007) and isolated/random topographic features (Egbert and

* Corresponding author.
E-mail address: rn2@princeton.edu (R.H. Nazarian).

http://dx.doi.org/10.1016/j.ocemod.2017.07.002

Ray, 2000; Buehler and Holmes-Cerfon, 2011; Legg, 2014) have been studied from both observational and modeling perspectives.

Despite their potential to be a sink of internal tidal energy, continental slope canyons have been largely overlooked by the modeling community. As Kunze et al. (2002) suggested, submarine canyons may indeed be significant sinks of internal wave energy due to both their frequency along the continental slope and their geometries. Given that about 10% of the continental slope is carved out by such canyons, and that the geometry of the canyons may be conducive to wave focusing, Carter and Gregg (2002) argued from their observations of Monterey Canyon that the internal wave energy dissipation and subsequent mixing is non-negligible (approximately the same order of magnitude as the mixing currently parameterized in ocean general circulation models) and warrants study in more depth. This conclusion is in agreement with other observational studies of internal wave-driven mixing in continental slope canyons (Gordon and Marshall, 1976; Hotchkiss and Wunsch, 1982; Gardner, 1989; Petruncio et al., 1998; Codiga et al., 1999; Bosley et al., 2004; Bruno et al., 2006; Lee et al., 2009a; 2009b; Xu and Noble, 2009; Gregg et al., 2011; Hall and Carter, 2011; Waterhouse et al., 2013; Vlasenko et al., 2016).

While our study is motivated by observations of mixing in actual continental slope canyons, we begin with idealized V-shaped canyons in order to tease out the fundamental dynamics (we further justify this choice of topography in Section 4). We develop and employ a ray tracing algorithm to explore the impact of canyon geometry on ray focusing and wave number within a linear context. While ray tracing algorithms have been used to understand internal wave dynamics before (Manders and Maas, 2004; Maas, 2005; Drijfhout and Maas, 2007; Rabitti and Maas, 2013; 2014), for the first time, we use reflection information to calculate the Froude number (formally defined in Section 3) and hence estimate the likelihood for instability. Thus, without the use of a fully-nonlinear general circulation model (GCM), we aim to predict, using our linear ray tracing algorithm, where regions of instability may occur for wave scattering off idealized, V-shaped canyon topography.

The idealized canyons we have chosen to analyze are oversimplifications of real canyon bathymetry; however canyons tend to follow a roughly V-shaped profile (Shepard, 1981) and our focus here is not to capture every detail of particular wave-topography interaction, but to explore the parameter space (Carter and Gregg, 2002). Specifically, we do a suite of experiments to vary the geometric parameters of the ratio of canyon mouth opening to canyon length, as well as the shape/thalweg (line of lowest elevation) slope, to understand the wave reflection behavior and resulting instability. These are two important geometric parameters which vary between observed continental slope canyons, and thus a good starting point for our study (Gregg et al., 2011; Hall and Carter, 2011). As a further simplification, we only consider remotely-generated M2 tidal-frequency, mode-one internal waves, a reasonable assumption as a sizable fraction of the internal wave energy is observed to be at the M2 tidal-frequency (Munk and Wunsch, 1998).

The goal of Part 1 of this study is to extend the internal wave reflection theory to 3D, rotated topography and to use this theory to construct a ray tracing algorithm. Our objective in designing this ray tracing is to follow a large number of rays through the canyon region as they reflect off the topography, and store information on the trajectory of these rays. This stored information then allows us to (i) predict regions where instability is energetically possible and (ii) understand the processes that cause these regions to experience instability. In Part 2, through a comparison with numerical simulations, we also seek to test the robustness of this ray tracing derived from the linear theory. This ray tracing will then be used in tandem with a fully nonlinear GCM to understand the topographic control on wave breaking and subsequent energy loss (Nazarian and Legg, 2017).

In this paper, we build upon existing internal wave reflection theory and use this theory as the backbone of our ray tracing algorithm to understand internal wave scattering in continental slope canyons. In Section 2, we present the physical theory of 3D wave reflection. Based on this theory, we develop the methodology used in the linear ray tracing algorithm in Section 3 and present examples of the ray tracing for various idealized topographies. This ray tracing code may be applied to internal wave scattering off any arbitrary topography, as the algorithm depends only on the local topographic parameters. We then present the idealized canyons, and the justification for such canyons, in Section 4. In Section 5 we analyze the results of the ray tracing algorithm for two classes of idealized continental slope canyons to obtain a first-order understanding of internal wave dynamics in continental slope canyons. We find that the linear ray tracing algorithm predicts large envelopes of both increased ray density and, for canyons with non-vertical sidewalls, an increase in vertical wave number, both of which can contribute to the formation of instabilities. We also find that this region of instability due to topographic focusing is modified by the spatial extent of the canyon, including the canyon height and relative canyon length. In Part 2 of this study we will add to this understanding by complimenting the ray tracing with a fully-nonlinear GCM, as well as using the GCM to test the robustness of the ray tracing algorithm (Nazarian and Legg, 2017).

2. Theory

When low mode internal waves are scattered by topography, energy can be effectively transferred to higher vertical wavenumbers, which leads to a higher Froude number. This nondimensional number, Fr, quantifies the stability of the flow and the likelihood of transitioning into the turbulent flow regime. We thus develop the 3D internal wave scattering theory applied to a rotated coordinate system to calculate the wavenumber as a function of the geometry of the topography by which it is scattered, as well as the original wave properties. The original theory of internal wave reflection off topography was set forth by Phillips (1963; 1966) and considered further by Eriksen (1982). We adapt the setup of Eriksen (hereafter E82) to a rotated coordinate system to construct the two symmetric sides of the V-shaped canyon.

We start by considering a plane slope, inclined at an angle, α, relative to the horizontal. We then rotate the plane by another angle, ζ, relative to the y-axis. These angles are displayed in Fig. 1 and the resulting inclined, rotated plane comprises one sidewall of our V-shaped canyon.

Similar to E82, we consider a semi-infinite domain with x denoting the onshore direction, y denoting the alongshore direction and z denoting the vertical (as seen in Fig. 1). We start with the linearized, inviscid, non-rotating Boussinesq equations and assume that nondivergence is satisfied. Our guiding equations can thus be written as:

$$\left.\begin{aligned} \frac{\partial u'}{\partial t} &= -\frac{1}{\rho_0}\frac{\partial p'}{\partial x} \\ \frac{\partial v'}{\partial t} &= -\frac{1}{\rho_0}\frac{\partial p'}{\partial y} \\ N^2 w' + \frac{\partial^2 w'}{\partial t^2} &= -\frac{1}{\rho_0}\frac{\partial^2 p'}{\partial t \partial z} \\ \frac{\partial u'}{\partial x} + \frac{\partial v'}{\partial y} + \frac{\partial w'}{\partial z} &= 0 \end{aligned}\right\} \tag{1}$$

where the prime notation denotes the wave perturbation fields. u, v and w are the velocity components in x, y and z, respectively, and p is the pressure. N^2 is the background density stratification, which is defined as $N^2 = -\frac{g}{\rho_0}\frac{\partial \rho}{\partial z}$, where ρ_0 is the background density.

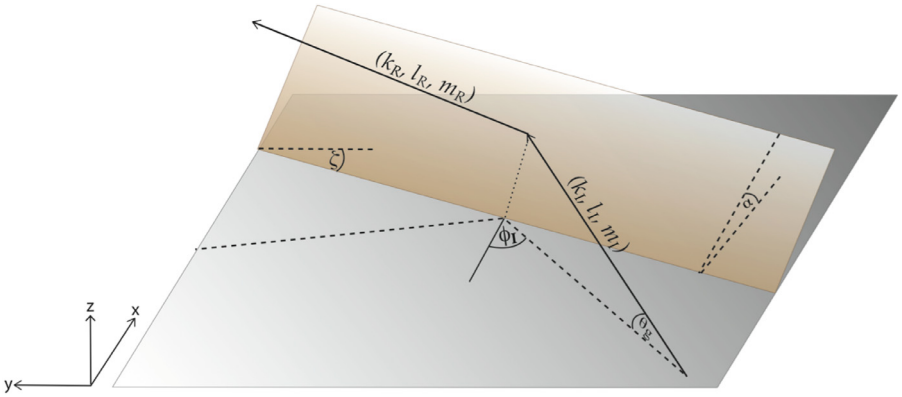

Fig. 1. Schematic of the wave reflection from sloping topography at an angle α to the horizontal, and rotated at an angle ζ from the y-axis. Bold arrows indicate the wave group velocity vectors. (k, l, m) are the wave vector components, and I subscripts denote the incident wave while R subscripts denote the reflected wave. The incident wave group velocity vector is at an angle θ_g to the horizontal, and an angle ϕ_I to the normal of the topographic plane. Based on the theory and schematic set forth in E82.

The system of four equations in four unknowns can be combined to derive an equation for the vertical velocity w':

$$\frac{\partial^2}{\partial t^2}\left(\frac{\partial^2}{\partial x^2}+\frac{\partial^2}{\partial y^2}+\frac{\partial^2}{\partial z^2}\right)w' + N^2\left(\frac{\partial^2}{\partial x^2}+\frac{\partial^2}{\partial y^2}\right)w' = 0 \tag{2}$$

Assuming a plane wave, decomposed into its incident and reflected components (indicated by I and R subscripts, respectively), the vertical velocity can be expressed as:

$$\begin{aligned} w' = {} & A_I \exp[i(k_I x + l_I y + m_I z - \omega z)] \\ & + A_R \exp[i(k_R x + l_R y + m_R z - \omega z)] \end{aligned} \tag{3}$$

where k, l and m are the onshore, alongshore and vertical components of the wavenumber, respectively, and ω is the wave frequency. A_I and A_R are the incident and reflected wave amplitudes. Alternatively, the wavenumber components can be written as $(k, l, m) = (K_H \cos(\phi+\zeta), K_H \sin(\phi+\zeta), m)$, where K_H is the horizontal component of the wave number, ϕ is the horizontal angle between the normal of the topography and wave vector and ζ is the angle of rotation of the inclined plane (again, following the E82 protocol and shown in Fig. 1).

Substituting (3) into (2) and applying the bottom boundary condition of no normal flow at $x = -(\tan\zeta)y + (\frac{\cot\alpha}{\cos\zeta})z$, the equality in (2) is satisfied if and only if

$$k_I \cos\zeta + l_I \sin\zeta + m_I \tan\alpha = k_R \cos\zeta + l_R \sin\zeta + m_R \tan\alpha \tag{4}$$

$$l_I \cos\zeta - k_I \sin\zeta = l_R \cos\zeta - k_R \sin\zeta \tag{5}$$

It should be noted that in the case of $\zeta = 0$, (4) and (5) simplifies to the case derived in E82 (i.e. with the setup of $l_I = l_R$).

We additionally know that the dispersion relation for internal waves can be expressed as

$$\tan^2\theta_I = \frac{m_I^2}{k_I^2 + l_I^2} = \frac{m_R^2}{k_R^2 + l_R^2} = \tan^2\theta_R = \frac{N^2-\omega^2}{\omega^2} \tag{6}$$

where the angle θ is the angle of the wave vector relative to the horizontal plane. It is related to the angle of the group velocity vector to the horizontal, θ_g, in Fig. 1 by the relation $\theta = \frac{\pi}{2} \pm \theta_g$. Combining the conservation of wavenumber equations, (4) and (5), as well as the dispersion relation, (6), we can solve for the reflected wavenumbers as a function of the incident wavenumber. Ignoring the solution of wave propagation through the bottom, we find:

$$\frac{m_R}{m_I} = -\frac{\cos(\alpha-\theta)}{\cos(\alpha+\theta)} - \frac{\sin(2\theta)\sin(2\alpha)(\cos(\phi_I)-1)}{2\cos(\alpha-\theta)\cos(\alpha+\theta)} \tag{7}$$

which is the same as derived in the non-rotated E82 case. Note that the subscripts are omitted for angle θ since the angle is conserved upon reflection. The horizontal components, k and l, however, differ from the E82 solution given that we have rotated the reference frame by angle ζ. The solution for each of these reflected wavenumbers yields a quadratic equation of the form $a_{k,l}x^2 + b_{k,l}x + c_{k,l} = 0$, where $x = (k_R/k_I), (l_R/l_I)$ and the coefficients, in standard notation, are expressed, respectively, as:

$$\left.\begin{aligned} a_k &= \sec^2(\zeta) \\ b_k &= 2\tan(\zeta)\tan(\phi_I+\zeta) - 2\tan^2(\zeta) \\ c_k &= \tan^2(\zeta) + \tan^2(\phi_I+\zeta) - 2\tan(\phi_I+\zeta)\tan(\zeta) \\ &\quad -\left(\frac{m_R^2}{m_I^2}\right)\sec^2(\phi_I+\zeta) \end{aligned}\right\} \tag{8}$$

and

$$\left.\begin{aligned} a_l &= \csc^2(\zeta) \\ b_l &= 2\cot(\zeta)\cot(\phi_I+\zeta) - 2\cot^2(\zeta) \\ c_l &= \cot^2(\zeta) + \cot^2(\phi_I+\zeta) - 2\cot(\phi_I+\zeta)\cot(\zeta) \\ &\quad -\left(\frac{m_R^2}{m_I^2}\right)\csc^2(\phi_I+\zeta) \end{aligned}\right\} \tag{9}$$

Again, notice that the ratio of the reflected wavenumber to the incident wave number reduces exactly to the E82 solution in the limit of $\zeta = 0$, as it should. The Eqs. (7)–(9) constitute a one-to-one relationship between the reflected and incident wavenumbers solely as a function of the wave and topographic properties; the utility of this relationship will be fully realized in Section 3 in the construction of a linear ray tracing algorithm. It should be stressed that although we have developed this theory with the intent of using it for continental slope canyons, it is generalizable to any arbitrary topography, as all topography can be described in terms of a local tangent plane characterized by the two angles, α and ζ.

For the problem of internal wave reflection, the relation between the wave slope and the topographic slope, known as the criticality, determines the directionality of the reflected ray. The criticality or steepness, s, of the topography is calculated as

$$s = \frac{|\tan\alpha|}{|\tan\theta_g|} \tag{10}$$

where α is the local angle of inclination relative to the horizontal and θ_g is the group velocity angle relative to the horizontal. When this relation is inserted into (10), and simplified using (6), we find that

$$s = \frac{|\tan\alpha|}{|\omega^2/(N^2-\omega^2)|} \tag{11}$$

When $s < 1$, the topography is referred to as subcritical, and rays undergo forward reflection. The converse is true for $s > 1$; that is the topography is termed supercritical and the rays reflect backwards. In the case of the topographic slope exactly matching that of the wave, the topography is deemed critical (i.e. $s = 1$). Slope criticality is the main differentiator between the different classes of canyons we consider in this study, and we return to it in Section 4.

3. Ray tracing algorithm

In order to understand the fundamental dynamics inside the idealized continental slope canyons or, more generally, wave reflection off any topography, a ray tracing algorithm is developed. Rays propagate throughout the domain based upon their group velocity, $c_g = (\partial\omega/\partial k,\ \partial\omega/\partial l,\ \partial\omega/\partial m)$ where ω is the internal wave frequency, which satisfies the dispersion relation (6). Thus, the internal wave group velocity can be expressed as:

$$c_g = \frac{N}{K}(\sin^2(\theta)\cos(\eta),\ \sin^2(\theta)\sin(\eta),\ -\sin(\theta)\cos(\theta)) \qquad (12)$$

where η is the horizontal angle, or mathematically, $\eta = \arctan(l/k)$, and K is defined as the resultant wavenumber (i.e. $K^2 = k^2 + l^2 + m^2$). If the stratification is constant (as it is in our idealized canyon study), the rays conserve wavenumber (and frequency) except during reflections. Since we do not consider Earth's rotation in this study, c_g has no f dependence, although f can be reinserted into the ray tracing algorithm by using the dispersion relation with rotation. As the wave numbers change upon reflection, so too the group velocity changes. Eq. (12) is multiplied by the time step, dt, to convert the group velocity to a ray propagation distance, i.e. $x(t + dt) = x(t) + c_g dt$.

In addition to needing values of α and ζ to evaluate the reflected wave numbers (7), (8) and (9), ϕ_I, the horizontal angle of the incoming ray relative to the horizontal normal line of the slope (see Fig. 1) is also required. This is the most time-consuming quantity to calculate since it depends on the orientation of the ray (i.e. quantity η) relative to the orientation of the slope (i.e. quantity ζ). Given that the sign of ϕ_I is important, we define ϕ_I to be positive if the topography's normal line is to the left of the incoming ray and negative if the topography's normal line is to the right of the incoming ray (e.g. $\phi_I > 0$ in Fig. 1).

Care must also be taken in calculating angle η after reflection. While the relations of (8) and (9) yield reflected wave numbers, and thus a value of η, this is only one possible value of η_R (for reference, we define this value as η_1). Specifically, the reflected value of η could be $|\eta_1|$, $-|\eta_1|$, $(|\eta_1| - \pi/2)$ or $(\pi/2 - |\eta_1|)$. We have developed a subroutine within the ray tracing algorithm to determine which value of η should be used. Namely, for every reflection two of the four values of η will lead to the ray propagating beneath topography. Given that this is unphysical, these two η options, which can vary for each case of reflection, are discarded. The final condition in choosing the reflected η is that the sign of ϕ_I must be the opposite of ϕ_R; that is, backward reflection is not allowed. The remaining value of η is then taken as η_R.

Rays are allowed to exit through all lateral boundaries and reflect back downwards from the sea surface. The wave numbers of each ray are diagnosed, as increases in the vertical wavenumber can lead to instability. The density of the rays is also tracked, as a high ray density, and thus high energy density, can also lead to instability. One property of the waves that we are not tracking is the phase. We are therefore not able to diagnose regions of constructive or destructive interference.

The ray tracing algorithm is illustrated for various continental slope topographies: a vertical wall (with both normally- and obliquely-incident rays), a subcritical slope and a supercritical slope in Figs. 2, 3, 4 and 5, respectively. For each case, only one ray is shown for clarity.

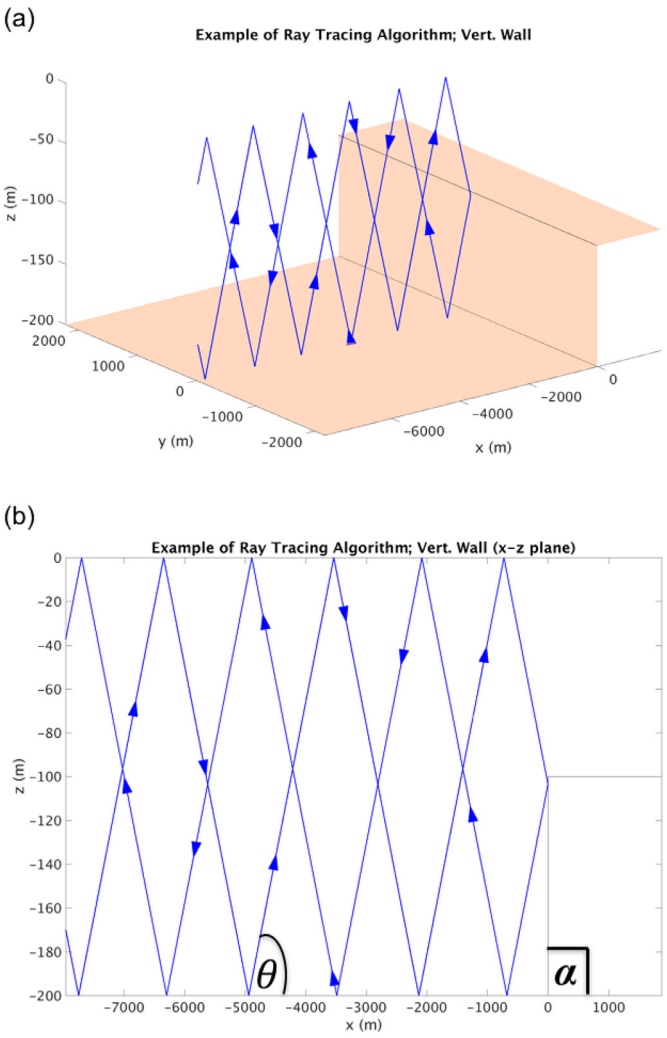

Fig. 2. Ray tracing algorithm application for a single rave propagating into the domain from the Western boundary, normal to topography, and reflecting off a vertical wall (i.e. $\alpha = 90°$). (a) 3-dimensional view of the ray propagation and reflection. (b) 2-dimensional view of the ray propagation and reflection in the x–z plane.

In our implementation of the ray tracing algorithm for continental slope canyons, the wave is initialized at the Western boundary (at $x = 0$) in the form of approximately 2000 rays, spread evenly over the y–z plane. For every initialization, there are both upward- and downward-going rays. Thus, we use our discrete ray tracing algorithm to accurately match the energy propagation of a continuous internal wave. The rays are tracing out the group velocity of the internal wave since we are interested in energy loss resulting from reflection, and tracing of phase is a secondary concern, and thus not included in the ray tracing algorithm. Although, for the purpose of our canyon study, the topography is idealized and known analytically, it is interpolated to a finer grid so that the ray tracing algorithm is generalizable to any input topography, such as that of an observed continental slope canyon. The ray tracing algorithm is also able to read bathymetry files that have nonuniform resolution and interpolate them onto an isotropic grid.

All rays are initialized with Eastward group velocity, although this initial condition can be customized to any arbitrary value. When rays interact with topography, be it the seafloor, shelf, or canyon, the new wave number components are calculated according to the three relations of (7), (8) and (9). The ray tracing algorithm calculates the point of reflection and does not allow the rays to propagate under the topography. Although it is known ex-

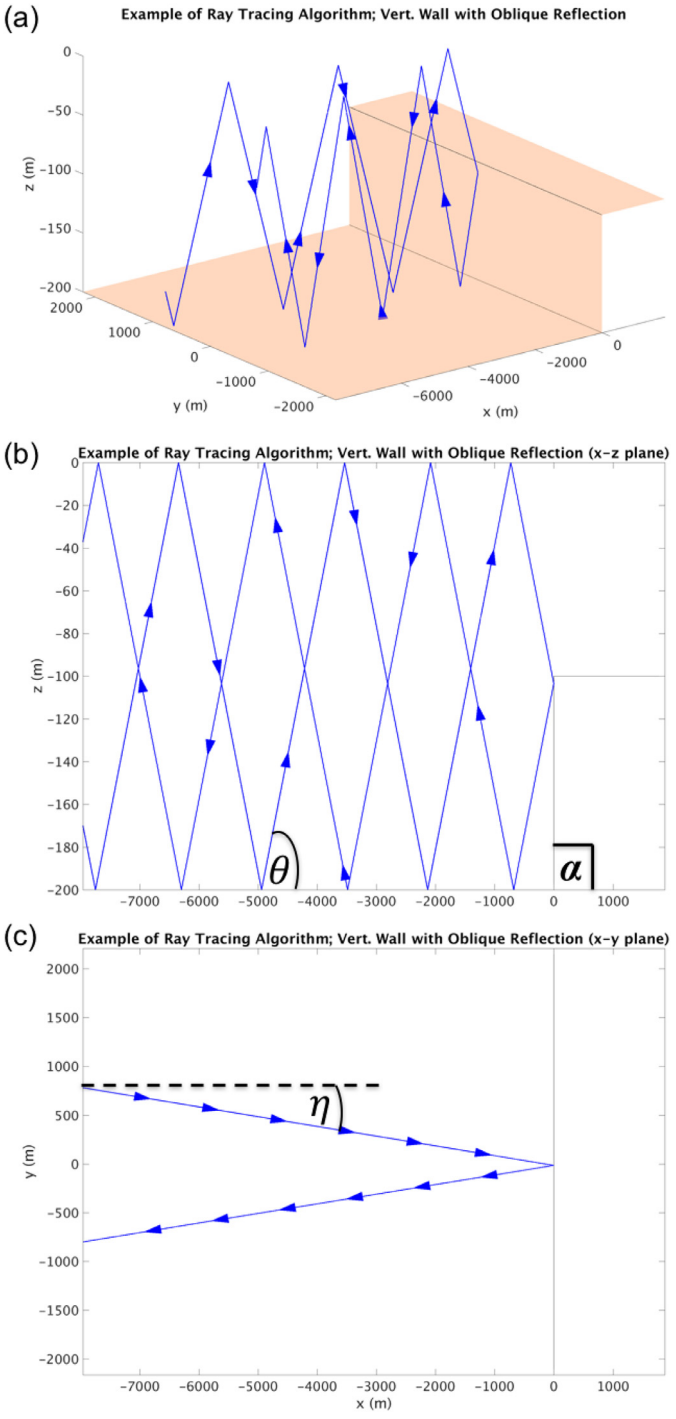

Fig. 3. Ray tracing algorithm application for a single rave propagating into the domain from the Western boundary, oblique to topography, and reflecting off a vertical wall (i.e. $\alpha = 90°$). (a) 3-dimensional view of the ray propagation and reflection. (b) 2-dimensional view of the ray propagation and reflection in the x–z plane. (c) 2-dimensional view of the ray propagation and reflection in the x–y plane.

actly for our idealized topography, the angle of vertical inclination, α, is calculated locally to make the algorithm as generalizable as possible. In its current form, ζ can be prescribed or calculated upon each reflection. Since the magnitude of ζ is constant for each canyon we consider in this study, we prescribe it for the canyons in this study since it reduces the ray tracing run time.

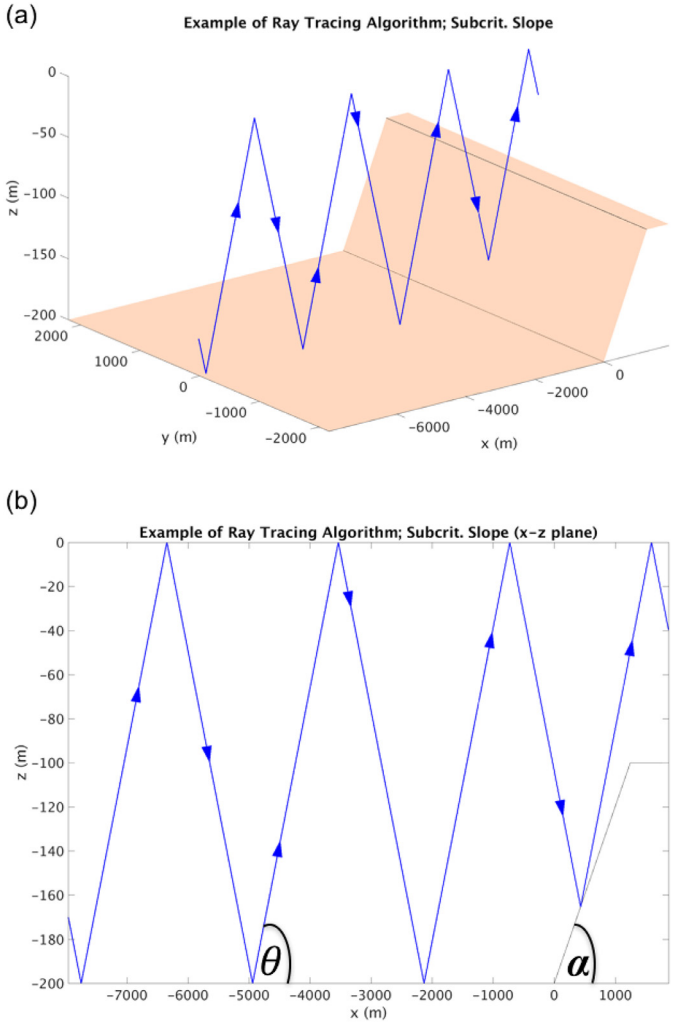

Fig. 4. Ray tracing algorithm application for a single rave propagating into the domain from the Western boundary, normal to topography, and reflecting off a subcritical slope. (a) 3-dimensional view of the ray propagation and reflection. (b) 2-dimensional view of the ray propagation and reflection in the x–z plane.

To quantify the potential for instability of the wave, we utilize the wave Froude number, canonically calculated as

$$Fr = \frac{U_H}{|c_{p,H}|} \tag{13}$$

where U_H is the maximum horizontal flow speed associated with the wave and $c_{p,H}$ is the horizontal phase speed and expressed as $(c_{p,x},\ c_{p,y}) = \frac{\omega}{k^2+l^2}(k,\ l)$. The Froude number indicates potential regions of instability if the ratio is greater than unity, or when the flow speed exceeds the phase speed. From the dispersion relation, (6), the phase speed in the denominator of (13) scales like

$$c_{p,H} = \sqrt{\left(\frac{\omega k}{k^2+l^2}\right)^2 + \left(\frac{\omega l}{k^2+l^2}\right)^2} = \frac{\omega}{\sqrt{k^2+l^2}} = \frac{\sqrt{N^2-\omega^2}}{m} \propto \frac{1}{m} \tag{14}$$

where the last equality is derived from the dispersion relation, (6). Therefore

$$Fr \propto \frac{U_H}{1/m} \tag{15}$$

The numerator of (13) can likewise be approximated. Assume that the wave fluxes some amount of energy along an infinite number

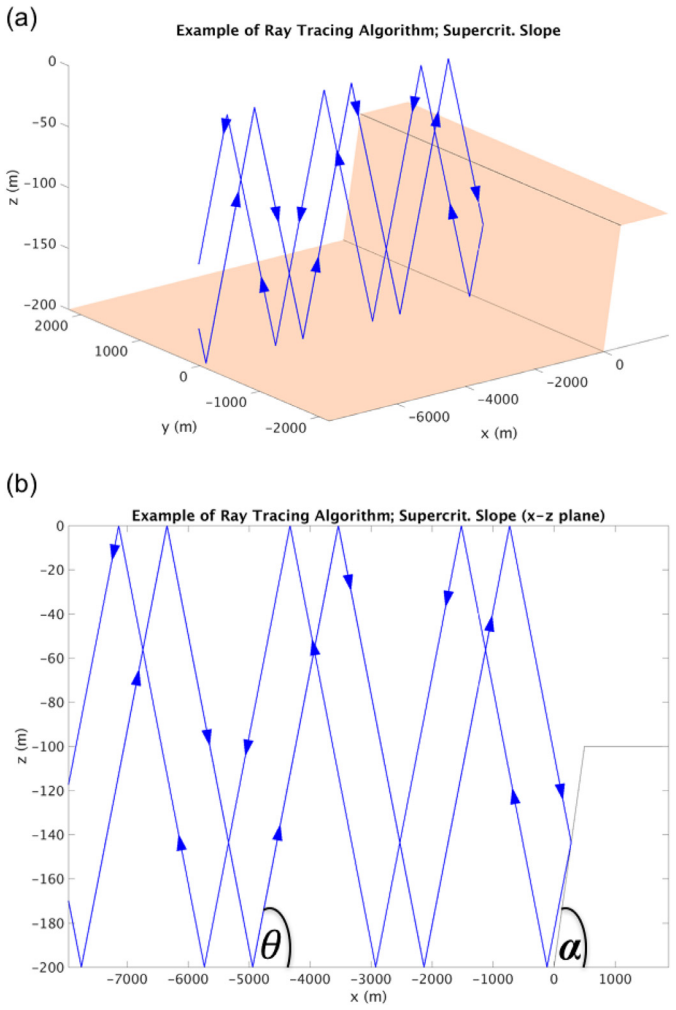

Fig. 5. Ray tracing algorithm application for a single rave propagating into the domain from the Western boundary, normal to topography, and reflecting off a supercritical slope. (a) 3-dimensional view of the ray propagation and reflection. (b) 2-dimensional view of the ray propagation and reflection in the x–z plane.

of rays, given by

$$\mathcal{F} = E \times c_g \tag{16}$$

where $\mathcal{F}$ is the energy flux per unit area, E is the energy density and c_g is the group velocity. If we assume that the total wave is decomposed into an infinite number of rays, then (16) can be rewritten in terms of individual rays as

$$\mathcal{F} = E_0 \times RD_A \times c_g \tag{17}$$

where RD_A is the ray density per unit area, diagnosable from the ray tracing (with units of number of rays per unit area) and E_0 is the energy per a single ray (i.e. a constant). If (17) is integrated over all space to include all rays, it will converge exactly to (16). Thus the energy density, E, can be expressed as

$$E = E_0 \times RD_A \tag{18}$$

If we multiply both sides of (18) by some arbitrary unit area, we find that the energy scales like the ray density. Given that the wave energy is equipartitioned between kinetic energy and potential energy,

$$KE \propto RD \tag{19}$$

where KE is the kinetic energy and RD is the ray density (with units of number of rays). Since the horizontal kinetic energy scales like U_H^2, (19) simplifies to

$$U_H^2 \propto RD \tag{20}$$

and thus, we can plug this into (15) and estimate the Froude number as

$$Fr \propto \frac{\sqrt{RD}}{1/m} \tag{21}$$

Therefore, the ratio of the reflected wave's Froude number to the incoming wave's Froude number can be taken exactly as

$$\frac{Fr_1}{Fr_0} = \left(\sqrt{\frac{RD_1}{RD_0}}\right) \times \left(\frac{m_1}{m_0}\right) \tag{22}$$

Note that RD_0 is the number of rays initialized at the Western boundary evaluated at the same depth as RD_1. Both RD_0 and RD_1 have units of number of rays per grid box. Taking the Froude number for the gravest (lowest) baroclinic internal tide from Legg (2014) (Fr_0 here, where $Fr_0 = \frac{U_0\pi}{H_0\sqrt{N^2-\omega^2}}$), we can solve for the maximum final Froude number in any given grid cell:

$$Fr_{1,max} = \left(\sqrt{\frac{RD_1}{RD_0}}\right)\left|\left(\frac{m_1}{m_0}\right)\right|_{max}\left(\frac{U_0\pi}{H_0\sqrt{N^2-\omega^2}}\right) \tag{23}$$

where U_0 and H_0 are the wave velocity amplitude and ocean depth at the Western boundary, respectively. Thus, for every grid cell in the ray tracing algorithm, we take the relative ray density and maximum vertical wave number to calculate the maximum Froude number. It is worth noting that, for our setup, $U_0 = 0.02$ m/s and $H_0 = 200$ m, leading to an initial Froude number of $Fr_0 = 0.32$. Thus, the wave is stable and will not break on its own; all breaking is the result of scattering off topography. While ray tracing algorithms have been used before to understand internal wave reflection (Manders and Maas, 2004; Maas, 2005; Drijfhout and Maas, 2007; Rabitti and Maas, 2013; 2014), the ray tracing algorithm that we develop is novel in that it uses the change in ray density and vertical wavenumber to estimate the maximum Froude number as a result of ray reflection. We present a synthesis plot of the ray tracing capabilities using an idealized continental slope canyon, the specific topography of interest in this study, after we introduce these canyons in Section 4.

4. Canyon setup

While this theory can be tested on any arbitrary topography, we have developed it to gain an understanding of internal wave dynamics in submarine canyons. Additionally, given that one of the variables the ray tracing algorithm uses to diagnose instability is ray density, canyons are an ideal testbed since they are one of the few topographies that can lead to changes in ray density due to 3D wave focusing effects. To construct the V-shaped canyons, we take two symmetric inclined planes and join them at the head (see Fig. 1). The first type of canyon we construct is the near-critical slope canyon, such that the center of the canyon is of near-critical slope. For the near critical slope canyon the thalweg steepness, $s_{thalweg}$, is 0.94, so the topographic slope is near-critical (recall that a steepness value of unity is considered critical) for our case of the M2-tidal frequency. This is constant for all canyons in the class, as the group velocity angle is dictated by the stratification and wave (tidal) frequency, both of which are held constant as well as $\alpha_{thalweg}$, which is also held constant. By construction, the sidewalls for the near-critical slope canyon are near-critical to supercritical (i.e. $\alpha = \alpha_{\text{near-critical}} \rightarrow 90^\circ$). A schematic of this type of canyon is shown in Fig. 6a. Critical and near-critical slopes have been the topic of numerous studies as they are conducive to enhanced mixing; upon reflection all wave rays are aligned alongslope. This high density of wave rays leads to a high energy density,

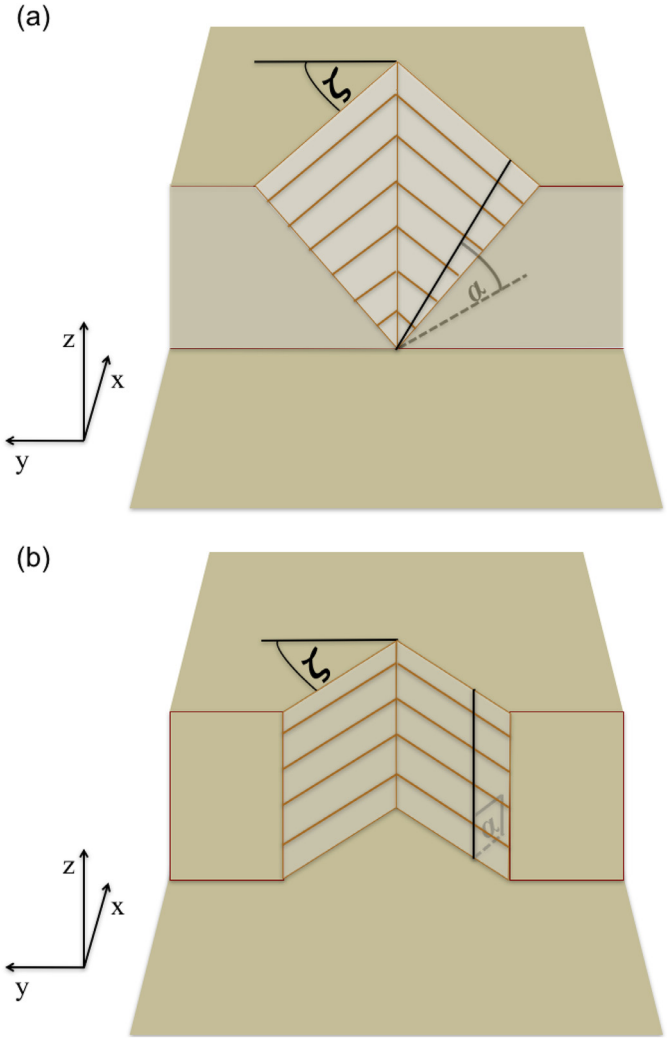

Fig. 6. Two classes of V-shaped canyons analyzed in this study. (a): near-critical slope canyon, (b): flat bottom canyon. Note that throughout our suite of experiments, angle ζ is varied identically for both class of canyons. Thus, the two different classes of V-shaped canyons are different in angle α only. The sidewalls of each canyon have isobaths, or lines of constant depth, drawn for clarity.

and thus the potential for instability, wave breaking, and subsequent mixing (Ivey and Nokes, 1989). It is thus possible that such a canyon could lead to enhanced levels of mixing.

The second class of V-shaped canyon constructed is a flat bottom canyon. In this case, the topography does not slope smoothly between the sea floor and continental shelf, as was the case for the near-critical slope canyon, but instead steps up at the V-boundary via a vertical wall. A schematic of this canyon can be found in Fig. 6b. The motivation behind the design of the canyon is that it possesses the potential to act as a wave trap for sufficiently large ζ (Maas et al., 1997). Note that both types of canyons have the same profile when viewed from the sea surface (i.e. in the x-y plane), but vary in their sidewall steepness (angle α) only. Throughout the suite of experiments, ζ is varied identically for both classes of canyons. For both classes of canyons, the canyon length, L, is held constant while the canyon mouth is altered to modulate ζ. Additionally, both classes of canyons have a maximum topographic height, H, that is only one-half of the total domain. Thus, we have established two differing values of α through the construction of these two types of V-shaped canyons, as well as a sweep of ζ, which is systematically varied for both cases.

Table 1
Summary of parameters of interest.

α	ζ (°)	H (m)	L (m)	ω^2 (10^{-8} s^{-2})	N^2 (10^{-6} s^{-2})
$\alpha_{near-critical}$	22.8	100	744	1.99	1.00
	48.3	100	744	1.99	1.00
	52.3	100	744	1.99	1.00
	64.4	100	744	1.99	1.00
	83.2	100	744	1.99	1.00
90°	22.8	100	744	1.99	1.00
	48.3	100	744	1.99	1.00
	64.4	100	744	1.99	1.00
	73.5	100	744	1.99	1.00
	73.5	150	744	1.99	1.00
	73.5	200	744	1.99	1.00
	73.5	100	1046.2	1.99	1.00
	73.5	100	1046.2	0.995	1.00
	83.2	100	744	1.99	1.00

While the two classes of canyons are differentiated by their value of α, α for the near-critical slope canyons has some ζ-dependence. That is, based on the construction of the topography,

$$\tan\alpha = \frac{\tan\alpha_t}{\cos\zeta} \tag{24}$$

such that for small values of ζ, the slope of the sidewalls is approximately the thalweg slope (i.e. $\tan\alpha \approx \tan\alpha_t$). As ζ increases, the sidewall slope increases to be larger than the thalweg slope. In the limit of $\zeta \to 90°$, the sidewall slope approaches vertical. There is thus a non-negligable ζ-dependence for the near-critical slope canyon sidewall steepness. This implies that the sidewall steepness for the near-critical slope canyons is near-critical to supercritical. It is thus preferable, and the approach of this paper, to differentiate canyons classes through their thalweg angle of inclination, α_t, which is held fixed for each canyon class.

To summarize, we have two classes of V-shaped canyons, that are distinguished only by their sidewall steepness, α. The first class of canyons has a thalweg steepness that is near-critical and so, by construction, near-critical to supercritical sidewalls. The second class of canyons has vertical walls, which are thus very supercritical. The second parameter of interest is the canyon aspect ratio, ζ, which is varied systematically for both canyons. We modulate ζ by adjusting the canyon width only. Both canyons have a fixed height, H, of 100 m and a fixed length, L, of 744 m. See Fig. 6 for the geometry of the two canyon classes. In Fig. 6, isobaths, or lines of constant depth, are overlaid on the sidewalls to make clear that the canyons vary in α. Parameters of interest, both topographic and those for the wave and ambient fluid, are listed in Table 1, as well as their corresponding values for the submarine canyons considered in this part of the study.

While these canyons follow idealized V-shape profiles with two different classes of sidewall steepnesses, their general profile is rooted in reality. In a statistical analysis of the occurrence of submarine canyons, Harris and Whiteway (2011) separated global submarine canyons into differing classes based on canyon geometry. They find that canyons surrounding New Zealand and Western North America have very small mean thalweg slopes (3.8 and 4.3°, respectively) and lie on active margins, which leads to steep sidewalls. These observed canyons are very similar to our flat bottom canyon class. They also find canyons, such as surrounding India and Australia that have larger thalweg slopes (ranging from 1.1 to 20.9° and 0.8 to 23.7°, respectively) which can be near-critical for certain wave frequencies. They observe these canyons to be on passive margins, which is indicative of more gradual sidewall slopes, akin to our near-critical slope canyon class. Thus, while certain simplifications have been used in the development of our topography, both classes of canyons are similar to submarine canyons observed

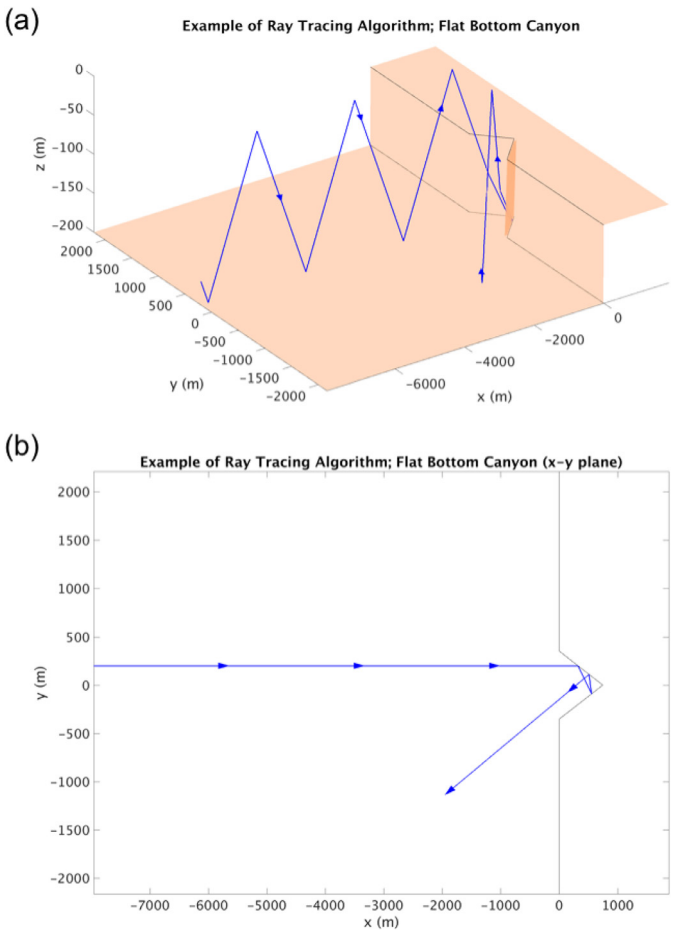

Fig. 7. An example of the ray tracing algorithm for a flat bottom canyon with $\zeta = 64.4^{\circ}$. (a): 3-dimensional perspective , (b): 2-dimensional perspective in the x–y plane (i.e. downward looking). A large number of rays are initiated at the Western boundary, spanning the x–z plane, with both upward and downward going components (only one ray is shown here for clarity). Rays then propagate Eastward according to the dispersion relation and can scatter off topography. Here the ray reflects off the canyon sidewall and enters onto the continental slope obliquely. As before, x is aligned with longitude (West to East) and y is aligned with latitude (South to North).

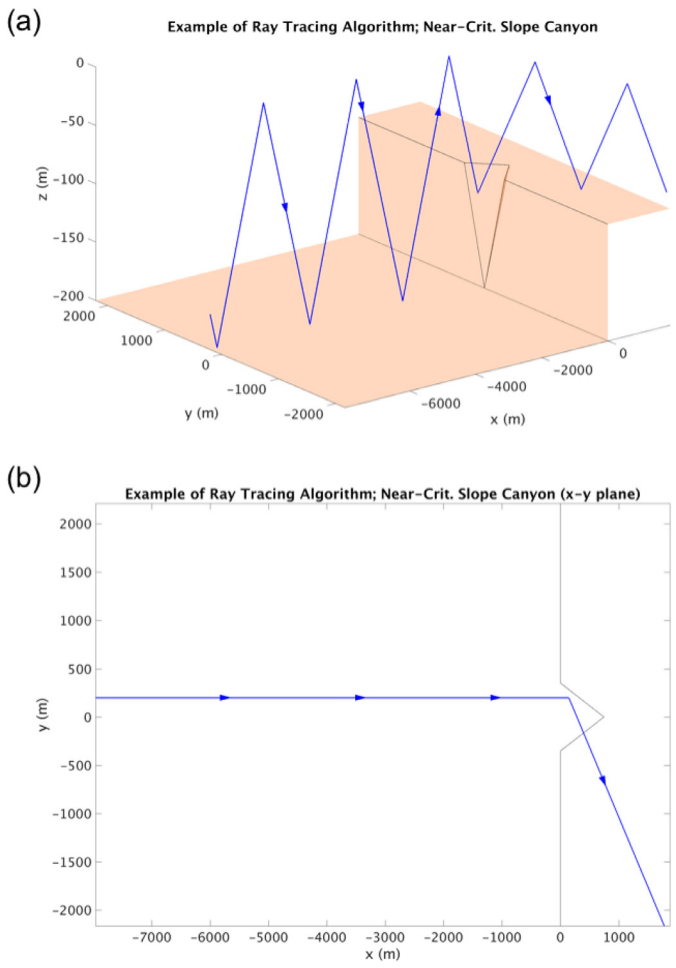

Fig. 8. As in Fig. 7, but now for the case of a near-critical slope canyon.

and there is the potential to apply the lessons learned in this idealized framework to real continental slope canyons. We will return to this in Part 2 of this study (Nazarian and Legg, 2017).

Now that we have defined our canyon classes, we present a schematic of internal wave reflection in flat bottom and near-critical slope canyons, similar to that presented for the cases of a vertical wall, subcritical slope and supercritical slope, in Figs. 7 and 8, respectively. Additionally, in Fig. 9, we present all of the calculations that can be conducted using the ray tracing algorithm, outlined in Section 3, for the case of a near critical slope canyon of moderate width.

5. Results

We now use the ray tracing algorithm to probe the parameter dependence of internal wave-driven instability in continental slope canyons. We start by considering the case of the flat bottom canyon and present individual ray trajectories and vertically-integrated relative increase in ray density for three different canyon aspect ratios in Fig. 10. We do not consider increases to the vertical wavenumber here, as the vertical wavenumber does not change upon reflection off vertical walls (see Section 2). Fig. 10 illustrates a ζ-dependence on the pattern of vertically-integrated increase in ray density.

For a relatively wide canyon, Fig. 10a-i illustrates that rays only reflect, at most, one time within the canyon region (some rays propagate over the canyon undisturbed). Additionally, all of these rays are then reflected out of the canyon. From geometric optics, we know that this is true for all flat bottom canyons with $\zeta < 30^{\circ}$. While the rays, and their associated energy, are able to exit the canyon without being trapped, the canyon does act to focus them toward the center, as seen in the relative ray density plot in Fig. 10a-ii. Since the vertical wavenumber cannot increase upon reflection, ray focusing is the only potential mechanism by which wave instability can be achieved in this framework.

In Fig. 10b, we consider a canyon of moderate width (i.e. $\zeta = 48.3^{\circ}$). Note that subsequent ray reflections inside the canyon are now possible. Again, from geometric optics, we know that at $\zeta = 45^{\circ}$ the second reflection must be further into the canyon. This is in contrast to the outward reflection of rays that characterizes the wide canyon in Fig. 10a. The magnitude of relative ray density per grid box is slightly enhanced in this regime, compared to the first regime and the pattern of increased ray density is more evenly distributed throughout the canyon region, leading to a higher concentration of ray energy. Additionally, note that this setup leads to wings of increased ray density extending outside the canyon region, a result of ray scattering and focusing. This can be an additional source for instability extending away from the topography, as the ray density can also be elevated, and thus lead to mixing, on the shelf.

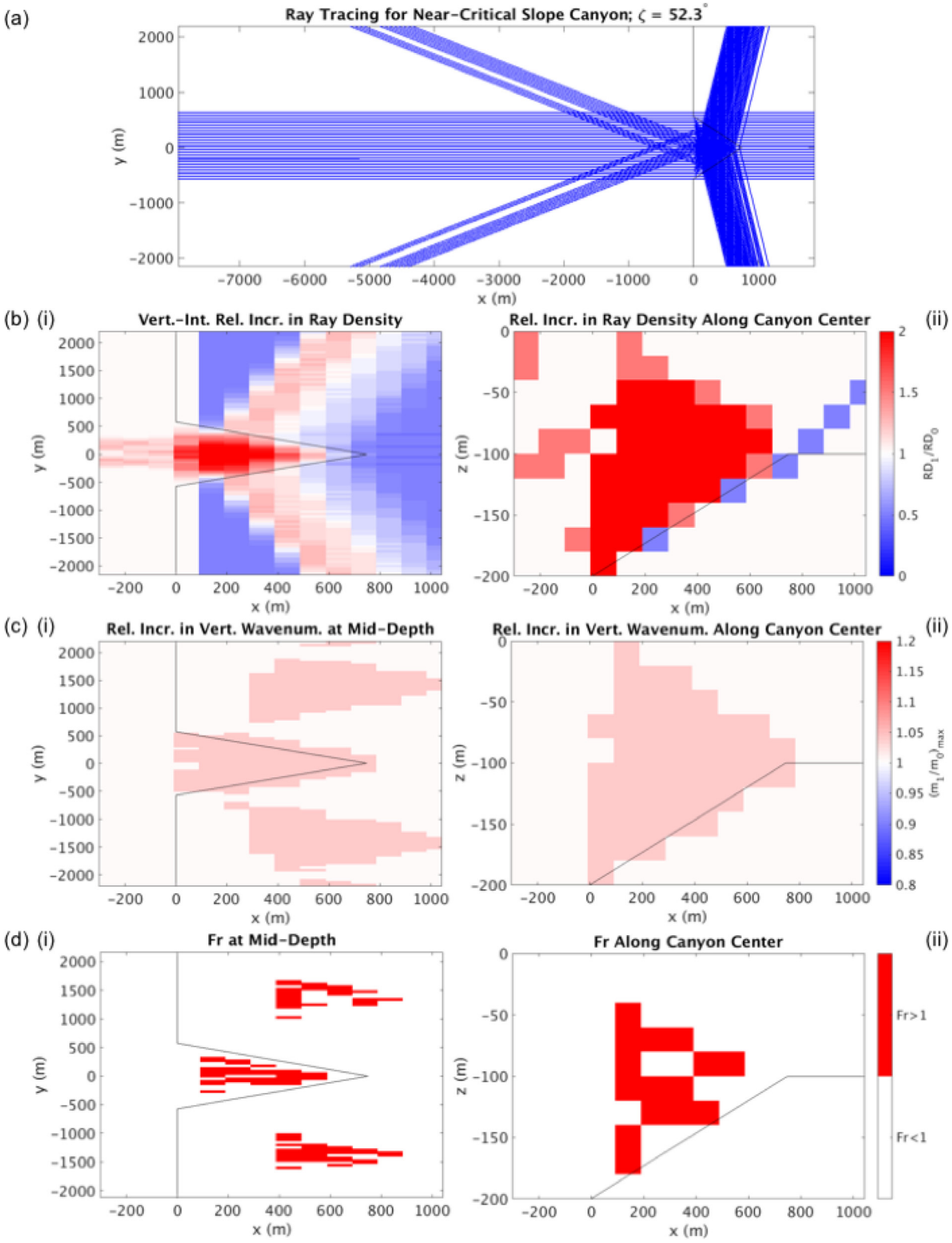

Fig. 9. Various diagnostics produced by the ray tracing algorithm for the case of a near-critical slope canyon with $\zeta = 52.3°$. Six hundred individual rays are used here for illustration, and thus individual rays are not distinguishable. (a) Ray tracing with 600 individual rays. (b-i) Relative increase in ray density, integrated in the vertical, and (b-ii) ray density in the *x*-*z* plane along the canyon center. (c-i and d-i) Relative increase in vertical wavenumber and maximum Froude number in the *x*-*y* plane at mid-depth, and (c-ii and d-ii) in the *x*-*z* plane along the canyon center, respectively. Notice here that $Fr > 1$ at various locations in the canyon, indicating potential regions of instability. Increased Froude number is also present for a given depth, indicating that instability can also occur on the shelf as a result of canyon processes. Given that the incoming wave has $Fr < 1$, this increase in Fr can be attributed to canyon effects.

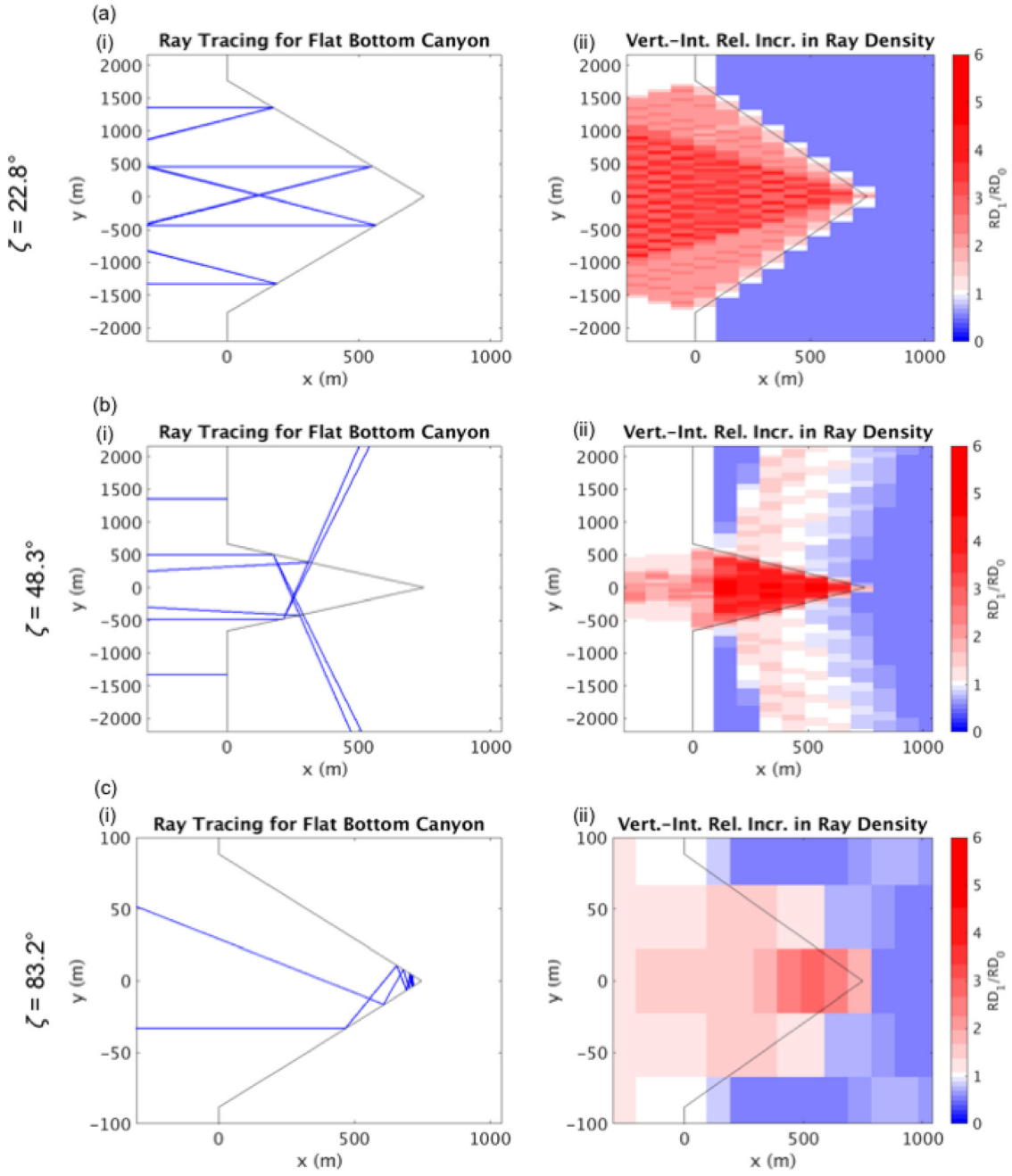

Fig. 10. Ray tracing (i) and ray density (ii) conducted for the case of the flat bottom canyon. The panels, from top to bottom, represent the cases of relatively large (a), moderate (b) and small (c) canyon width, respectively. The ray tracing plots only show a limited number of rays to illustrate the reflection patterns, while the ray density plots are the result of a large number of both upward- and downward-going rays spanning all of y and z, initiated at the Western boundary. Note that panel (c) is zoomed in due to the canyon being very narrow.

Fig. 10c illustrates the case of a narrow flat bottom canyon. For this instance, it is possible for rays entering the canyon region to have multiple reflections and remain trapped in the canyon, leading to high ray/energy density as in canyons of more moderate width (i.e. Fig. 10b). Yet, the ray tracing output illustrates that very few rays are able to enter the canyon region due to the decreasing mouth width corresponding to increasing ζ. This is potentially a mitigating factor in how much energy can be concentrated in flat bottom canyons for large values of ζ.

Despite having a different thalweg slope, α_t, we find that the near-critical slope canyon case behaves similarly to the case of the flat bottom canyon (Figs. 11a and 12a). The main distinction between the near-critical slope canyon and flat bottom canyon is that the sidewalls are not vertical in the case of the near-critical slope canyon, which allows a change/redistribution of wavenumber upon reflection, as outlined in Section 2. The main implication of this physics is that, for relatively wide canyons experiencing, at most, one reflection ($\zeta < 30°$), the rays are still scattered out of the canyon upon reflection, but onto the shelf. This is in contrast to the flat bottom canyon case, in which rays are scattered back out towards the abyss (see Fig. 10a).

We next consider the case of a slightly narrower canyon, again with $\zeta = 48.3°$ in Figs. 11b and 12b. For the case of the near-critical slope canyon, the transition point for outward scattering and secondary reflections no longer occurs at $\zeta = 30°$ due to the non-vertical sidewalls. Instead, the transition point is shifted towards

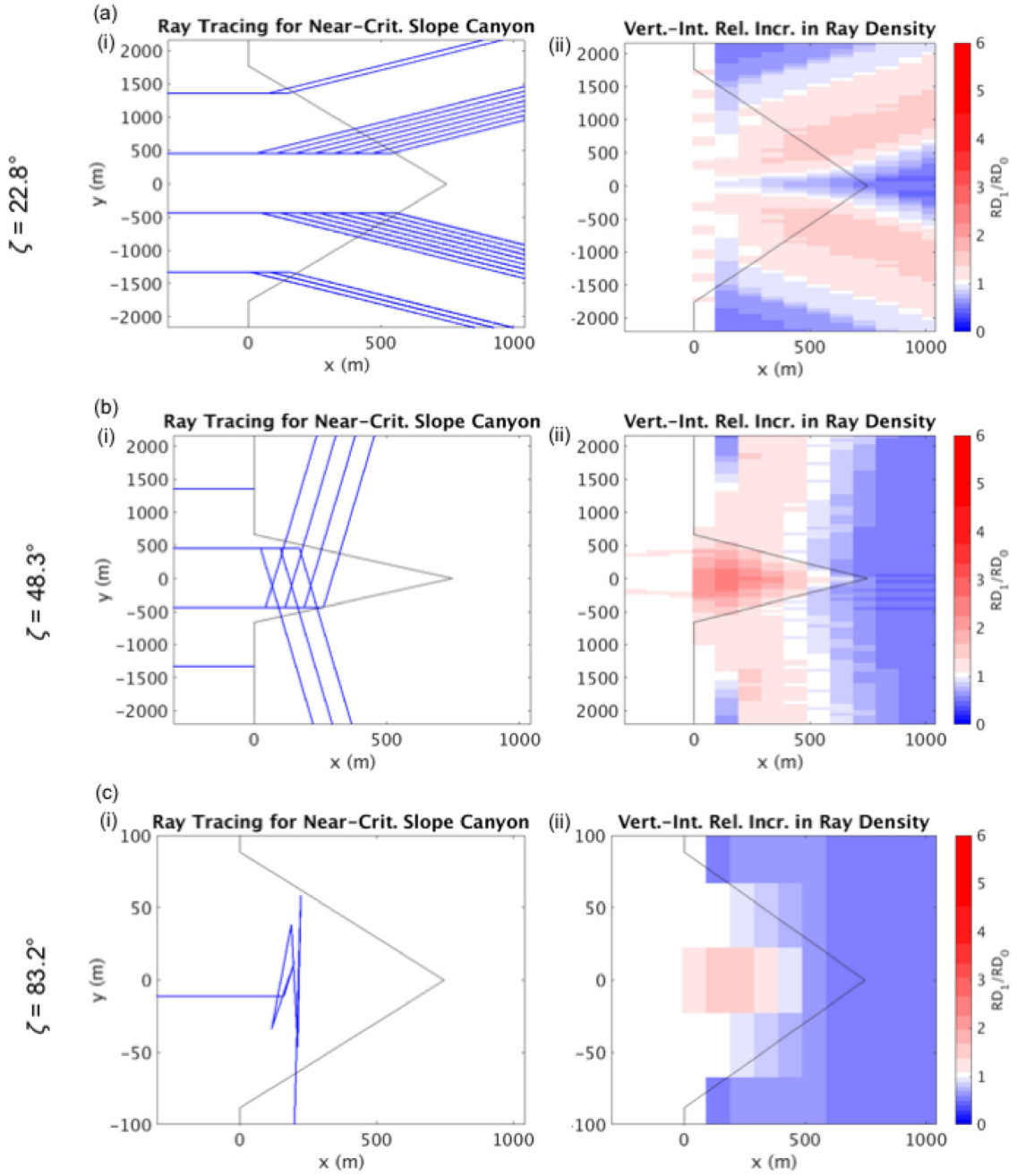

Fig. 11. Ray tracing (i) and ray density (ii) conducted for the case of the near-critical slope canyon. The panels, from top to bottom, represent the cases of relatively large (a), moderate (b) and small (c) canyon width, respectively. The ray tracing plots only show a limited number of rays to illustrate the reflection patterns, while the ray density plots are the result of a large number of both upward- and downward-going rays spanning all of y and z, initiated at the Western boundary. Note that panel (c) is zoomed in due to the canyon being very narrow.

higher ζ. This is a direct implication of the dispersion relation and the redistribution of wavenumber components upon reflection off the topography. At this higher transition point, all rays are scattered further into the canyon. This threshold is derived from Eq. (8). Specifically, rays begin to be reflected into the canyon at the transition of $k_R = 0$, and thus the quadratic equation with variable k_R/k_I simplifies to

$$\tan^2(\zeta) + \tan^2(\phi_I + \zeta) - 2\tan(\phi_I + \zeta)\tan(\zeta) - \left(\frac{m_R^2}{m_I^2}\right)\sec^2(\phi_I + \zeta) = 0 \tag{25}$$

We know that for the initial reflection, ϕ_I can either be $\pm\zeta$ based on which side of the canyon the ray reflects off. Both positive and negative values of ϕ_I yield the same solution so, for ease, we use $\phi_I = -\zeta$ which renders (25)

$$tan^2(\zeta) = \left(\frac{m_R}{m_I}\right)^2 \tag{26}$$

where the ratio of the vertical numbers is given in (7). This yields a transitional ζ of 45.3°, which is confirmed by the ray tracing algorithm. While the point of transition is shifted, the same underlying physics is present: rays are now reflected back into the canyon region where they can further reflect and scatter. As the number of reflections increases, so too does the likelihood of increasing vertical wavenumber and, potentially, breaking. There also continue to be wings of enhanced ray density extending from the canyon re-

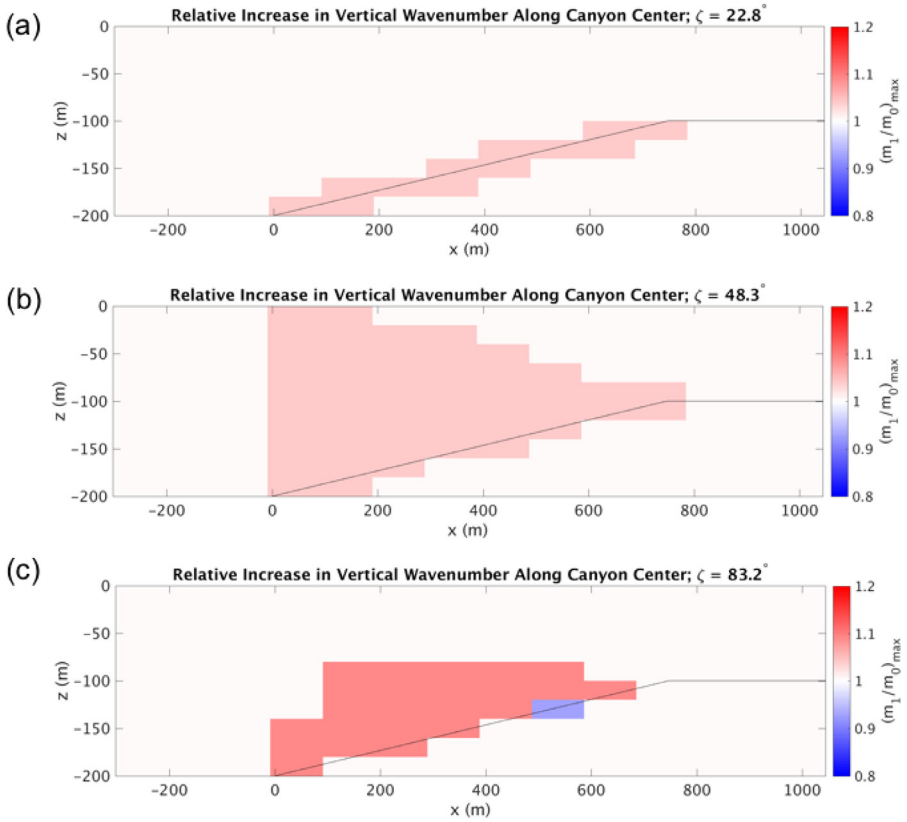

Fig. 12. As in Fig. 11, except now the maximum ratio of reflected vertical wave number to incident vertical wave number is plotted along the canyon center, as the vertical wave number can change within a near-critical slope canyon.

gion, another result of the canyon ray scattering. Additionally, the increase in vertical wave number, another precursor for potential instability, is more pronounced and encompasses a larger spatial area, for this higher ζ canyon (see Fig. 12b).

For large values of ζ, Figs. 11c and 12c suggest that narrow near-critical slope canyons show a significantly smaller region of wave focusing and increased vertical wavenumber than narrow flat bottom canyons and thus, potentially less mixing. This is due to the fact that the ray density in the near-critical slope canyons decreases much faster as a function of ζ than that of the flat bottom canyon, which can be seen in a comparison of Figs. 10 and 11. Although the ray density decreases rapidly and the envelope of increased vertical wavenumber has shrunk, the magnitude of the increase in vertical wavenumber increases to a greater extent compared to near-critical slope canyons of moderate ζ, thus potentially mitigating some of the effects of decreased wave focusing. These three near-critical slope canyon cases are summarized in Figs. 11 and 12 in a similar fashion to Fig. 10.

So far we have only used the ray tracing to consider variations in two topographic parameters: the canyon aspect ratio (i.e. ζ) and the thawleg slope (i.e. α_t). Given the relative speed of the ray tracing algorithm versus a fully-nonlinear numerical model, we can also use the ray tracing algorithm to probe the sensitivity of our results to the topographic quantities that we have hitherto held constant: canyon height, H, and canyon length, L. To complete this test, we conduct the ray tracing for the case of the flat bottom canyon with $\zeta = 73.3^\circ$, as the ray tracing algorithm suggests this is where the ray density for flat bottom canyons is at a maximum and we are interested in how changes to these parameters can make the canyon more or less effective at leading to wave instability. We only consider the flat bottom canyon here, as changing the height of the near-critical slope canyon implies an increase in the canyon length, and we want to separate the height and length dependence.

First, we investigate the implication of increasing the canyon height, the results of which are shown in Fig. 13. As the canyon height increases from the default value of 100 m (Fig. 13a) to the full depth of the domain, 200 m (i.e. from sea floor to sea surface, Fig. 13c), the vertically-integrated ray density increases. Thus, taller canyons are more efficient at focusing and, potentially, trapping internal wave energy. Given that the only mechanism for instability in the flat bottom canyon is increased ray density, we would expect this increase in canyon height to lead to an increased potential for instability. Qualitatively, Fig. 13 suggests that the ray density within the canyon and outside the canyon mouth, and therefore the instability within the canyon and outside the canyon mouth, increases linearly with increasing canyon height. An appropriate scaling for the height-dependence of the instability and potential for energy loss in canyons may thus be estimated as H/D where H is the height of the canyon and D is the full domain depth. In the case of Fig. 13c, this ratio is equal to unity. Perhaps intuitive, this scaling is important when transferring this understanding to fully-nonlinear GCMs where canyon height is one of the important differentiating factors between canyons. Also note that this scaling is valid for canyons with critical and supercritical side slopes, but not for subcritical side slopes which lead to forward wave scattering and propagation onto the shelf.

We similarly test the sensitivity of wave focusing in canyons to the length of the topography. We again consider the case of the $\zeta = 73.5^\circ$ flat bottom canyon and now consider the Froude number as it provides more intuition when considering slices in the x–z plane than does the ray density at each depth. The Froude number from the default (i.e. $H = 100$ m) ray tracing calculation is shown in Fig. 14a. The default length of the canyon for all simu-

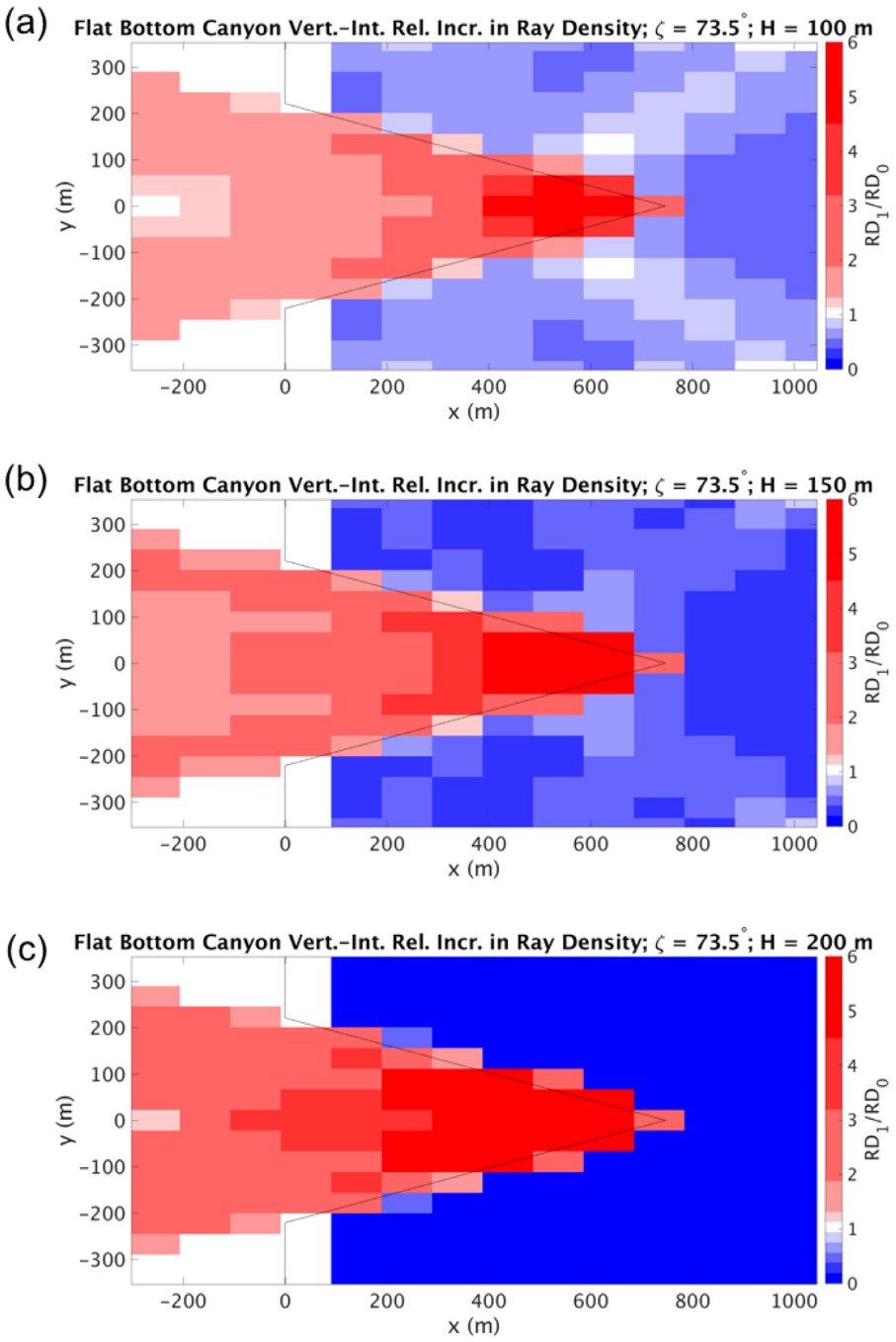

Fig. 13. Vertically-integrated relative increase in ray density for a flat bottom canyon with height 100 m (a), 150 m (b) and 200 m (c). As the canyon height increases, canyons become more efficient at focusing and, potentially, trapping internal wave energy.

lations was 744 m (see Table 1). We elongate the canyon to a length of 1046.2 m (roughly 1.4 times longer than the default canyon), as well as increase the canyon width, so that ζ remains fixed at 73.5°. The result is shown in Fig. 14b. There is a marked increase in the spatial extent of Fr >1 for the longer canyon. In the default case, the horizontal extent of the region of potential instability was approximately 400 m, while for the elongated canyon the region of potential instability is approximately 600 m (this approximation of a 50% increase in the extent of instability is in approximate agreement with the factor of 40% increase in the canyon length). The vertical extent of instability remains relatively constant. There is also an increase in the magnitude of the Froude number in the potentially unstable regions. Thus, this sensitivity test suggests that the potential energy lost from the internal wave due to the canyon may scale like parameter L, the length of the canyon.

Note, however, that it is not the absolute length of the canyon that is important, but the canyon length relative to the wavelength of the internal tide. Between Fig. 14a and b, the wavelength is fixed for the gravest baroclinic internal tide, but if the wave were of a different frequency, and thus a different wavelength, we may expect more or less of the wave to interact with and reflect off the canyon topography. This hypothesis is tested in Fig. 14c. As the wavelength is doubled, the spatial extent of the potential instability decreases by approximately a factor of one half. The magnitude of the Froude number in the regions of potential instability is also reduced. This suggests that the energy loss in the canyon region

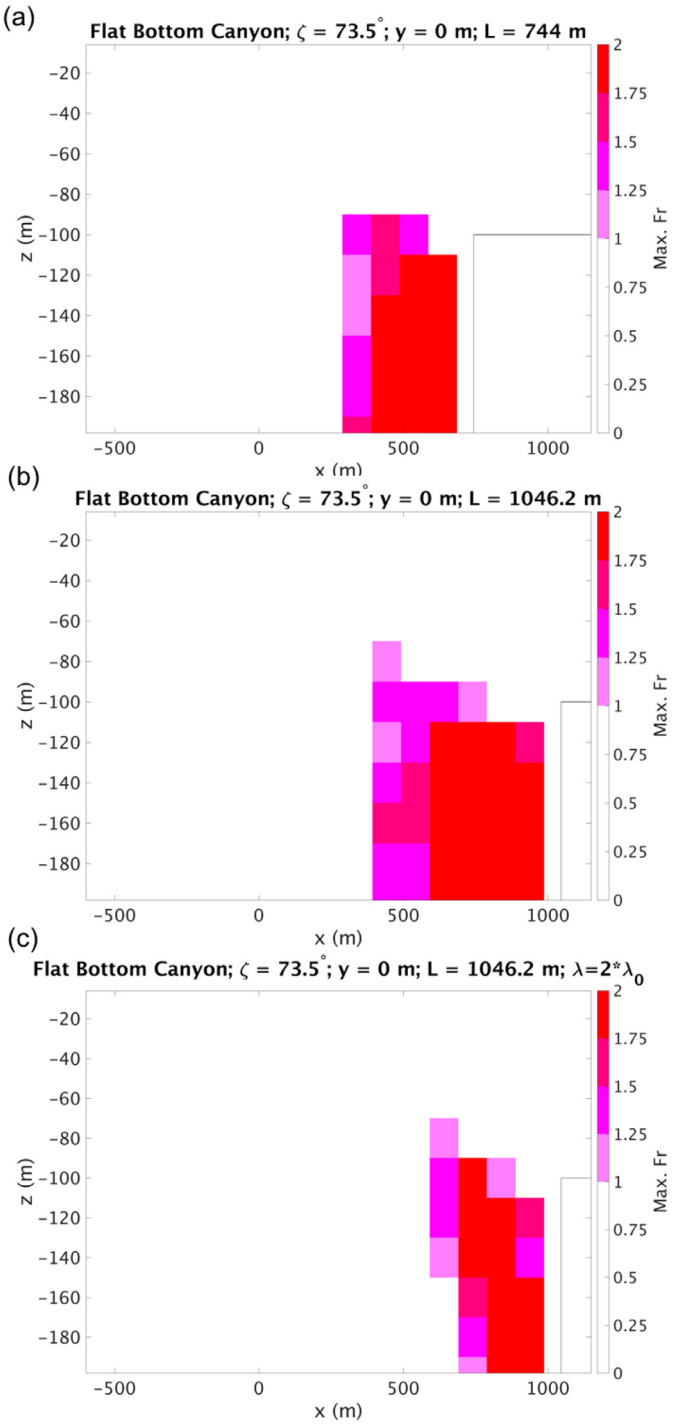

Fig. 14. Maximum Froude number from the ray tracing algorithm, taken along the center of a flat bottom canyon in the second regime. (a) Flat bottom canyon of the default length of 744 m and (b) flat bottom canyon of the new length of 1046.2 m and (c) flat bottom canyon of the new length of 1046.2 m with double the frequency of that in (a) and (b). For all canyons, ζ remains constant at 73.5°. Note the variation in the colorbar now for Fr >1. (For interpretation of the references to color in this figure legend, the reader is referred to the web version of this article.)

may thus scale like L/λ_x where λ_x is the horizontal component of the wavelength aligned with the canyon axis. We hypothesize that this scaling is likewise appropriate for the near-critical slope canyon but we do not test that here, as we can only differentiate the effects of changing canyon height and length by considering the case of vertical sidewalls.

6. Discussion and conclusion

There have been extensive numerical modeling studies regarding internal tide energy loss at a variety of topographic features, yet submarine canyons, specifically canyons on the continental slope, have not received sufficient attention. As a first attempt to study the underlying physical processes and understand the topographic parameters that govern the strength of canyon-induced mixing, we have developed a ray tracing algorithm from the linear theory to be used on two classes of idealized continental slope canyons. This ray tracing algorithm tracks quantities such as ray density and wave number. From these quantities, we have developed an estimate of the Froude number, which is a measure of the likelihood of instability and mixing. This is the first time that a ray tracing algorithm has been used to estimate the Froude number and the likelihood of instability resulting from internal wave reflection off topography.

In the construction of this ray tracing algorithm from the linear theory, we have not made any assumptions that are canyon specific; we have simply extended the internal wave reflection theory to some 3D rotated, inclined plane (with parameters α and ζ). This algorithm could therefore be applied to wave reflection off any arbitrary topography, since the patch of topography that a ray reflects off can, on some infinitesimal level, be considered a 3D rotated, inclined plane. The ray tracing may, in the future, be used as a precursor to a GCM or observational campaign, to identify whether instabilities occur for given topography and where those instabilities occur. The ray tracing algorithm does not require significant computational power or time and may thus be a powerful tool in considering whether GCM-scale simulations or field programs should be conducted, as well as the scope of such simulations or observations.

Here we have provided numerous examples of the utility of the ray tracing algorithm for continental slope canyons, in addition to showing its generalizability for other topographies. Perhaps contrary to intuition, we have observed that canyons of intermediate aspect ratio are most efficient at increasing ray, and thus energy, density, which can thereby lead to mixing. Although the threshold for subsequent reflections in the canyon is different between the flat bottom ($\zeta = 30^\circ$) and the near-critical slope canyons ($\zeta = 45.3^\circ$), both canyon classes exhibit an increase in ray density for moderate width canyons (i.e. for canyons with $L \propto W$, where W is the canyon width). Additionally, for the case of near-critical slope canyons, certain values of ζ can lead to a 15% or larger increase in vertical wavenumber, and thus a decrease in the vertical length scale, functioning as another potential catalyst for instability. We have also tested the sensitivity of our results based on the default values of canyon height and length. Informed by the ray tracing algorithm for the case of a flat bottom canyon with some existing instability present in the default case, we conducted further experiments with slightly modified values of H, L, and λ_x. Based on the changes to the spatial scales of potential instability, we proposed that canyon instability and energy loss can be scaled by H/D and L/λ_x. This is one direct way that the ray tracing can inform parameterizations for tidally-driven mixing in continental slope canyons in GCMs.

So far, we have not offered any test of robustness that the ray tracing algorithm correctly predicts regions of instability in continental slope canyons. Our goal in this paper is to document the formation of a ray tracing approach and employ it to obtain a first-order understanding of internal wave scattering dynamics in continental slope canyons. In Part 2 of this study (Nazarian and Legg, 2017), we compare our ray tracing results with calculations of instability diagnosed from a fully-nonlinear GCM as a means of testing the ray tracing's robustness. Additionally, we combine the utility of the ray tracing algorithm and the utility of a GCM

to further explore the idealized parameter space that we have developed here. Used in tandem, these two approaches allow us to gain a deeper understanding of the effects of canyon sidewall slope and canyon aspect ratio in regulating internal wave-driven mixing within and around canyons.

Acknowledgments

The authors thank Stephen Griffies and Robert Hallberg for reviewing early versions of this manuscipt, two anonymous reviewers for their helpful comments as well as Angelique Melet and Ben Mater for insightful conversations. This report was prepared by Robert Nazarian under award NA08OAR4320752 from the National Oceanic and Atmospheric Administration, U.S. Department of Commerce. The statements, findings, conclusions, and recommendations are those of the authors and do not necessarily reflect the views of the National Oceanic and Atmospheric Administration or the U.S. Department of Commerce.

References

Alford, M., MacKinnon, J., Nash, J., Simmons, H., Pickering, A., Klymak, J., Pinkel, R., Sun, O., Rainville, L., Musgrave, R., Beitzel, T., Fu, K.-H., Lu, C.-W., 2011. Energy flux and dissipation in luzon strait: two tales of two ridges. J. Phys. Oceanogr. 41, 2211–2222.

Bosley, K., Lavelle, J., Brodeur, R., Wakefield, W., Emmett, R., Baker, E., Rehmke, K., 2004. Biological and physical processes in and around astoria submarine canton, oregon, USA. J. Marine Syst. 50, 21–37.

Bruno, M., Vazquez, A., Gomez-Enri, J., Vargas, J., Lafuente, J., Ruiz-Canavante, A., Mariscal, L., Vidal, J., 2006. Obersvations of internal waves and associated mixing phenomena in the portimao canyon area. Deep-Sea Res. 53, 1219–1240.

Buehler, O., Holmes-Cerfon, M., 2011. Decay of an internal tide due to random topography in the ocean. J. Fluid Mech. 678, 271–293.

Cacchione, D., Wunsch, C., 1974. Experimental study of internal waves over a slope. J. Fluid Mech. 66, 223–239.

Carter, G., Gregg, M., 2002. Intense, variable mixing near the head of monterey submarine canyon. J. Phys. Oceanogr. 32, 3145–3165.

Codiga, D., Renouard, D., Fincham, A., 1999. Experiments on waves trapped over the continental slope and shelf in a continuously stratified rotating ocean. J. Marine Res. 57, 585–612.

Drijfhout, S., Maas, L., 2007. Impact of channel geometry and rotation on the trapping of internal tides. J. Phys. Oceanogr. 37, 2740–2763.

Egbert, G., Ray, R., 2000. Significant dissipation of tidal energy in the deep ocean inferred from satellite altimeter data. Nature 405, 775–778.

Eriksen, C., 1982. Observations of internal wave reflection off sloping bottoms.. J. Geophys. Res. 87, 525–538.

Gardner, W., 1989. Periodic resuspension in baltimore canyon by focusing of internal waves. J. Geophys. Res. 94, 18185–18194.

Gordon, R., Marshall, N., 1976. Submarine canyons: internal wave traps? Geophys. Res. Lett. 3, 622–624.

Gregg, M., Hall, R., Carter, G., Alford, M., Lien, R.-C., Winkel, D., Wain, D., 2011. Flow and mixing in ascension, a steep, narrow canyon. J. Geophys. Res. 116 (C7).

Hall, R., Carter, G., 2011. Internal tides in monterey submarine canyon. J. Phys. Oceanogr. 41, 186–204.

Hall, R., Huthnance, J., Williams, R., 2013. Internal wave reflection on shelf-slopes with depth-varying stratification. J. Phys. Oceanogr. 43, 243–258.

Hallock, Z., Field, R., 2005. Internal-wave energy fluxes on the new jersey shelf. J. Phys. Oceanogr. 35, 3–12.

Harris, P., Whiteway, R., 2011. Global distribution of large submarine canyons: geomorphic differences between active and passive continental margins. Marine Geo. 285, 69–86.

Hotchkiss, F., Wunsch, C., 1982. Internal waves in hudson canyon with possible geological implications. Deep-Sea Res. 29, 415–442.

Ilicak, M., Vallis, G., 2012. Simulations and scaling of horizontal convection. Tellus A 64 (18377).

Ivey, G., Nokes, R., 1989. Vertical mixing due to the breaking of critical internal waves on sloping boundaries. J. Fluid Mech. 204, 479–500.

Johnston, T., Merrifield, M., 2003. Internal tide scattering at seamounts, ridges, and islands. J. Geophys. Res. 108 (3180).

Johnston, T., Rudnick, D., Carter, G., 2011. Internal tidal beams and mixing near monterey bay. J. Geophys. Res. 116 (C03017).

Klymak, J., Buijsman, M., Legg, S., Pinkel, R., 2013. Parameterizing baroclinic internal tide scattering and breaking on supercritical topography: the one- and two-ridge cases. J. Phys. Oceanogr. 43, 1380–1397.

Klymak, J., Moum, J., Nash, J., Kunze, E., Girton, J., Carter, G., Lee, C., Sanford, T., Gregg, M., 2006. An estimate of tidal energy lost to turbulence at the hawaiian ridge. J. Phys. Oceanogr. 36, 1148–1164.

Kunze, E., MacKay, C., McPhee-Shaw, E., Morrice, K., Girton, J., Terker, S., 2012. Turbulent mixing and exchange with interior waters on sloping boundaries. J. Phys. Oceanogr. 42, 910–927.

Kunze, E., Rosenfeld, L., Carter, G., Gregg, M., 2002. Internal waves in monterey submarine canyon. J. Phys. Oceanogr. 32, 1890–1913.

Lee, I.-H., Lien, R.-C., Liu, J., Chuang, W.-S., 2009a. Turbulent mixing and internal tides in gaoping (kaoping) submarine canyon, taiwan. J. Marine Syst. 76, 383–396.

Lee, I.-H., Wang, Y.-H., Liu, J., Chuang, W.-S., Xu, J., 2009b. Internal tidal currents in the gaoping (kaoping) submarine canyon. J. Marine Syst. 76, 397–404.

Legg, S., 2014. Scattering of low-mode internal waves at finite isolated topography. J. Phys. Oceanogr. 44, 359–383.

Legg, S., Adcroft, A., 2003. Internal wave breaking at concave and convex continental slopes. J. Phys. Oceanogr. 33, 2224–2246.

Legg, S., Klymak, J., 2008. Internal hydraulic jumps and overturning generated by tidal flow over a tall steep ridge. J. Phys. Oceanogr. 38, 1949–1964.

Maas, L., 2005. Wave attractors: linear yet nonlinear. Int. J. Bifurcat. Chaos Appl. Sci. Eng. 15, 2757–2782.

Maas, L., Benielli, D., Sommeria, J., Lam, F., 1997. Observation of an internal wave attractor in a confined, stably stratified fluid. Nature 388, 557–561.

MacKinnon, J., Alford, M., Sun, O., Pinkel, R., Zhao, Z., Klymak, J., 2013. Parametric subharmonic instability of the internal tide at 29 degrees n. J. Phys. Oceanogr. 43, 17–28.

Manders, A., Maas, L., 2004. On the three-dimensional structure of the interial wave field in a rectangular basin with one sloping boundary. Fluid Dyn. Res. 35, 1–21.

Munk, W., Wunsch, C., 1998. Abyssal recipes ii: energetics of tidal and wind mixing. Deep-Sea Res. 45, 1977–2010.

Nash, J., Alford, M., Kunze, E., Martinit, K., Kelly, S., 2007. Hot-spots of deep mixing on the oregon continental slope. Geophys. Res. Lett. 34.

Nazarian, R.H., Legg, S., 2017. Internal wave scattering in continental slope canyons, Part 2: A comparison of ray tracing and numerical simulations. Ocean Model. in press.

Nikurashin, M., Legg, S., 2011. A mechanism for local dissipation of internal tides generated at rough topography. J. Phys. Oceanogr. 41, 378–395.

Petruncio, E., Rosenfeld, L., Paduan, J., 1998. Observations of the internal tide in monterey canyon. J. Phys. Oceanogr. 28, 1873–1903.

Phillips, N., 1966. The equations of motion for a shallow rotating atmosphere and the “traditional appximation”. J. Atmosp. Sci. 23, 626–628.

Phillips, O., 1963. Energy transfer in rotating fluid by reflection of internal waves. Phys. Fluids 6, 513–520.

Rabitti, A., Maas, L., 2013. Meridional trapping and zonal propagation of intertial waves in a rotating fluid shell. J. Fluid Mech. 729, 445–470.

Rabitti, A., Maas, L., 2014. Inertial wave rays in rotating spherical fluid domains. J. Fluid Mech. 758, 621–654.

Shepard, F., 1981. Submarine canyons: multiple causes and long-time persistence. AAPG Bull. 65, 1062–1077.

St. Laurent, L., Nash, J., 2004. An examination of the radiative and dissipative properties of deep ocean internal tides. Deep-Sea Res. 51, 3029–3042.

Talley, L., 2013. Closure of the global overturning circulation through the indian, pacific and southern oceans: schematics and transports. Oceanography (80–97).

Vlasenko, V., Stashchuk, N., Inall, M., Porter, M., Aleynik, D., 2016. Focusing of baroclinic tidal energy in a canyon. J. Geophys. Res. 121, 2824–2840.

Waterhouse, A., MacKinnon, J., Nash, J., Alford, M., Kunze, E., Simmons, H., Polzin, K., St. Laurent, L., Sun, O., Pinkel, R., Talley, L., Whalen, C., Huussen, T., Carter, G., Fer, I., Waterman, S., Naveira Garabato, A., Sanford, T., Lee, C., 2014. Global patterns of diapycnal mixing from measurements of turbulent dissipation rate. J. Phys. Oceanogr. 44, 1854–1872.

Waterhouse, A., Tutak, B., Valle-Levinson, A., Sheng, Y.-P., 2013. Influence of two tropical storms on the residual flow in a subtropical tidal inlet. Estuaries Coasts 36, 1037–1053.

Xu, J., Noble, M., 2009. Currents in monterey submarine canyon. J. Geophys. Res. 114 (C3).